Water Management
Volume 165 Issue WM10

Quadtree flood simulations with sub-grid digital elevation models
Stelling

ice | proceedings

Proceedings of the Institution of Civil Engineers
Water Management 165 November 2012 Issue WM10
Pages 567–580 http://dx.doi.org/10.1680/wama.12.00018
Paper 1200018
Received 29/01/2012 Accepted 02/05/2012
Keywords: floods & floodworks/hydraulics & hydrodynamics/information technology

ICE Publishing: All rights reserved

ice Institution of Civil Engineers publishing

Quadtree flood simulations with sub-grid digital elevation models

Guus S. Stelling
Professor, Faculty of Civil Engineering and Geosciences, Delft University of Technology, Delft, the Netherlands; Visiting Professor, Faculty of Engineering, National University of Singapore, Singapore

Flooding is an increasing hazard to society and good governance now implies careful water management in terms of design, planning and control of urban and rural areas. This requires that rainstorms, extreme water levels and so on are taken into account with relevant precision. A great aid is the existence of graphical information systems with raster-based digital elevation models (DEMs). Modern technology such as Lidar means that DEMs are of ever-increasing resolution. This paper describes how, without adaptations, a DEM can be used efficiently for detailed 2D flooding simulations. The method is based on four components: the sub-grid method; bottom friction derived from the divided channel method; the finite-volume staggered grid method for shallow water equations with rapidly varying flows; and quadtrees.

1. Introduction

Cartesian grids have many advantages; for example, simple numerical equations are involved and generating suitable meshes is relatively quick and can be fully automated. However, accurate representation of arbitrary land–water boundary outlines is often a problem. Land–water interfaces vary in type. For example, steep walls (such as in quays and dykes) do not move in space as the water level changes and in situations such as these, finite elements and unstructured grids might give a better solution. However, for land–water boundaries that move horizontally as well, such as tidal flats, river banks with mildly sloping bottoms or overland flow, every method faces similar problems.

Recent decades have seen a resurgence of Cartesian grids for computational fluid dynamics. Their classical disadvantage has been largely removed by proposing flow solvers (e.g. cut cells, immersed boundary method, quadtrees) that deal with moving and arbitrary boundaries (e.g. Aftosmis *et al.*, 1998; Causon and Ingram, 2001; Mittal and Iaccarino, 2005; Rosatti *et al.*, 2005). Another recent development is raster-based digital elevation models (DEMs) of ever-increasing resolution, which have been applied in flood simulations (e.g. Bates and De Roo, 2000; Horritt and Bates, 2001; Marks and Bates, 2000). In some works, detailed bathymetric data are used as a sub-grid (Bates, 2000; Yu and Lane, 2006a, 2006b), taking into account some kind of porosity (Cea and Vazquez-Cendon, 2010; Sanders *et al.*, 2008). The effect on bottom friction of sub-grid depth variation inside a coarse grid cell might be accounted for by the definition of the so-called 'effective depth' (Defina, 2000; Yu and Lane, 2006b). Casulli (2009) and Casulli and Stelling (2011) apply detailed sub-grid data in combination with unstructured grids, both for 2D and 3D flow equations. This approach combines the advantages of accurate representation of both sharp and mild land–water interfaces. Casulli (2009) explains the non-linearity of the continuity equation due to the sub-grid combined with flooding and drying. Brugnano and Casulli (2009) give a rigorous proof of convergence of the Newton method for a sparse system of non-linear equations if the wet surface is a non-decreasing function of the water level. Flooding problems may contain different flow types within one domain, such as overland flow and rapidly varying flow due to dam break and/or dam overflow. Rapidly varying flow is often simulated with Godunov-type methods (Begnudelli *et al.*, 2008; Cea and Vazquez-Cendon, 2010; Liang *et al.*, 2004). These methods, however, are often not very efficient for overland flow and flow in deeper water due to explicit time integration and time-consuming computational procedures on non-staggered grids. Stelling and Duinmeijer (2003), Kramer and Stelling (2008) and Kernkamp *et al.* (2011) describe a semi-implicit method that is reasonably accurate and efficient for a variety of situations such as rapidly varying flow, overland flow and flow in normal conditions such as rivers, estuaries and coastal seas.

This paper attempts to combine the best components from the aforementioned literature. The proposed method is based on four components

(*a*) the sub-grid method, including flooding and drying (Casulli, 2009)
(*b*) bottom friction based on the concept of roughness depth, described in this paper
(*c*) the finite-volume staggered grid method for shallow water equations with rapidly varying flows (Stelling and Duinmeijer, 2003), including semi-implicit time integration (Casulli and Walters, 2000)
(*d*) quadtrees (e.g. Wang *et al.*, 2004).

The method is outlined in Section 2. First, the grids are defined and then the integration of a fine raster grid, the DEM, with a Cartesian coarse grid is described. For this goal, indicator functions are used to obtain approximating step functions with a continuous domain. The result is suitable for the application of a finite-volume method. The local variation of the bottom within a coarse grid cell requires special attention for friction. For overland flow, this is a dominant aspect of the momentum balance. The notion of roughness depth is defined to account both for depth and roughness variation. Advection of momentum, which is applicable to rapidly varying flows such as dam overflow, is also treated. This section also describes the implicit time integration including the non-linear implicit equations with flooding and drying. The examples in Section 3 show that a sufficiently refined sub-grid can represent both sharp and soft land–water interfaces with satisfactory accuracy, similar to cut cells. Section 4 presents concluding remarks and the appendix explains how tables can be constructed to save memory and computation time.

2. Numerical method

The 2D shallow water equations are as follows. The continuity equation is

$$h_t + (uh)_x + (vh)_y = 0 \tag{1}$$

Momentum in the x-direction is given by

$$u_t + uu_x + vu_y + g\zeta_x + \frac{c_f}{h}u\|u\| = 0 \tag{2}$$

and the momentum equation in the y-direction is

$$v_t + uv_x + vv_y + g\zeta_y + \frac{c_f}{h}v\|u\| = 0 \tag{3}$$

in which

$$h(x, y, t) = \zeta(x, y, t) - e(x, y)$$

denotes the total water depth, $u(x, y, t)$ and $v(x, y, t)$ are depth-averaged velocities, g is acceleration due to gravity, $\zeta(x, y, t)$ is the water level above reference plane, $e(x, y)$ is the bottom elevation above reference plane and c_f denotes a dimensionless friction function.

The starting point of the numerical method is a detailed Cartesian grid or DEM (see Figure 1). For the computation of water levels, the DEM pixels are clustered into larger cells, as shown in Figures 2–4. The cells may have different sizes, since they are

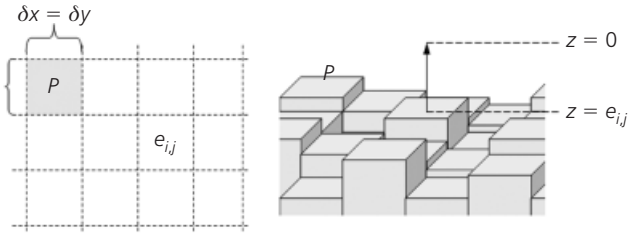

Figure 1. Digital elevation model as a step function

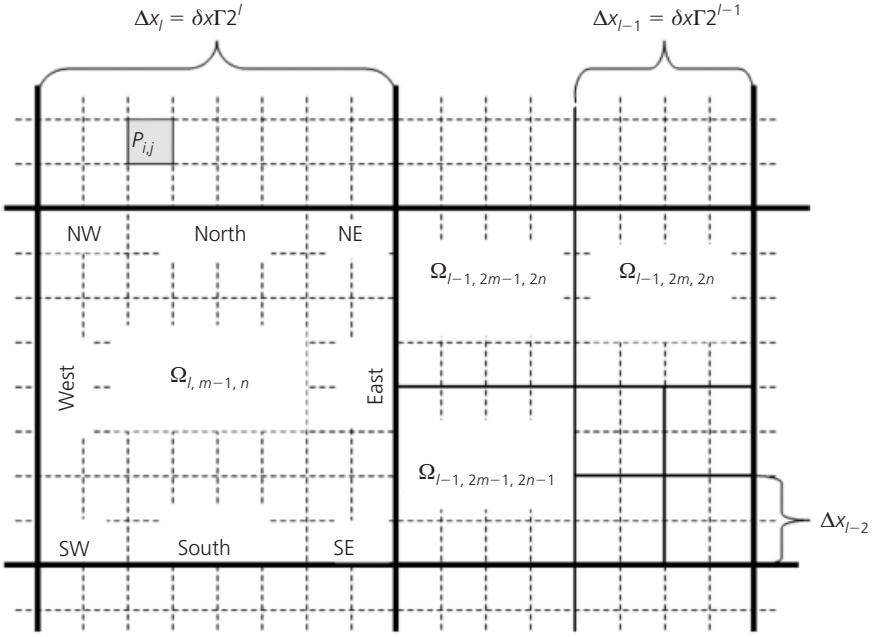

Figure 2. Quadtree coarse grid domain

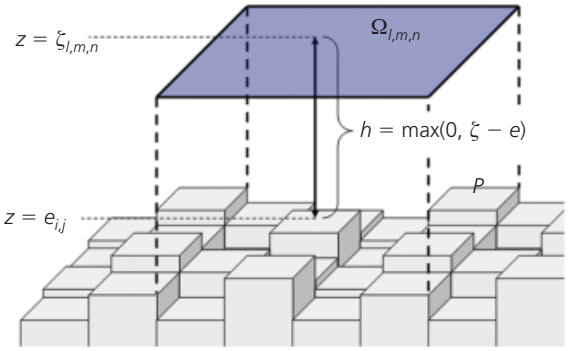

Figure 3. Finite volume with sub-grid

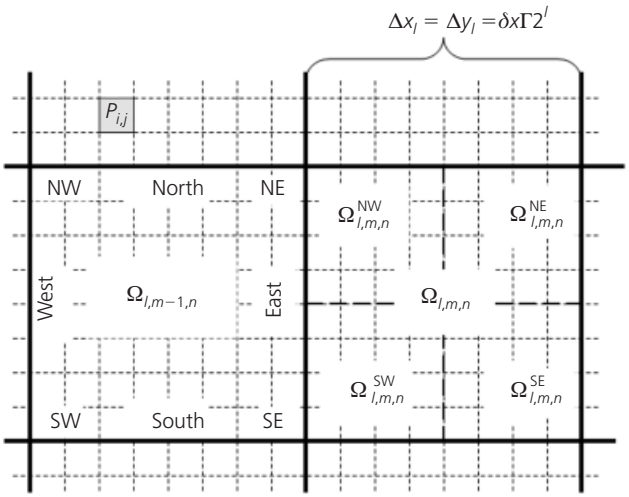

Figure 4. Coarse grid sub-domains

ordered according to a quadtree (Figure 5). Here, a finite-volume method is used in a rigorous way, so the continuity equation is solved strictly mass-conservative and also the momentum equation is solved strictly momentum-conservative. The grid is staggered so that there are different mass volumes and momentum volumes. The mass volumes are centred around the leaves of

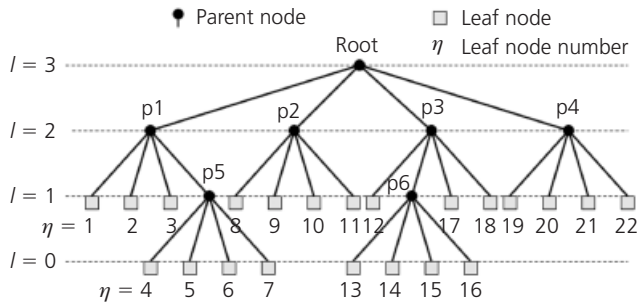

Figure 5. Hierarchical quadtree ordering

the quadtree. The momentum volumes are centred around the interfaces of two adjacent leaf cells (see Figure 6). This implies that if the adjacent cells are of equal size, the momentum cell is composed of one half of each cell. If the adjacent cells have a different size, then the momentum cell is composed of one quarter of the largest cell and one half of the smallest cell (Figures 6 and 7). It turns out to be very efficient to use the quarters of a leaf cell, denoted by the compass direction (Figure 4), as the basis for the approximation of both bottom friction and momentum transport. All this is explained, with mathematical details, in the following subsections.

2.1 Integration of sub-grid with coarse grid

The sub-grid idea is based on two grids with different resolution. Bottom values are given in a fine Cartesian grid or DEM (Figure 1). The size of a DEM pixel is defined by $\delta x \times \delta x$. Water levels and velocities have a coarse grid Cartesian quadtree domain (Figure 2). The coarse grid sizes are a multiple of δx given by $\Delta x_l = \Gamma\, \delta x\, 2^l$; Γ and l are integers,

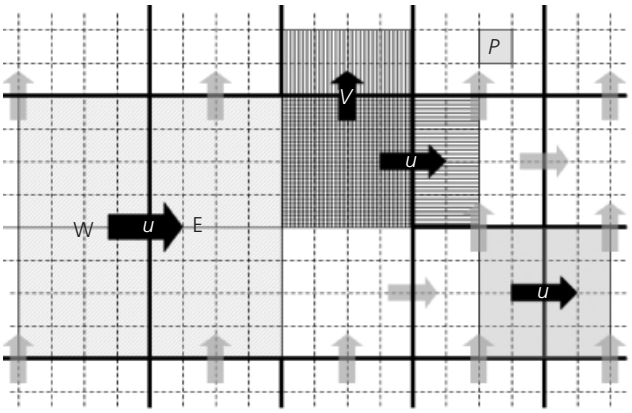

Figure 6. Finite-volume velocity domains in coarse grid

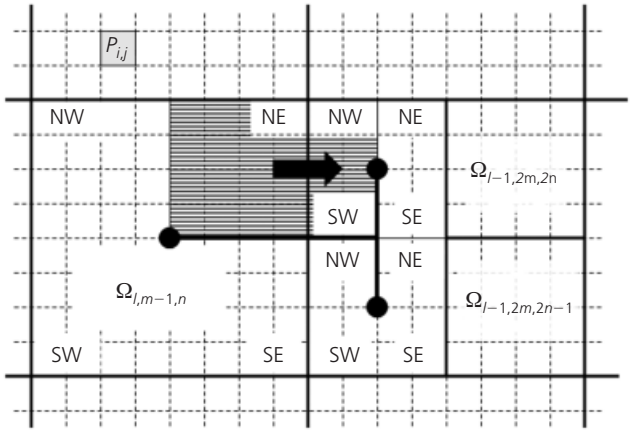

Figure 7. Pressure gradient stencil in quadtree

$\Gamma \geqslant 1$ and $l \geqslant 0$. Each coarse grid cell can be considered as a cluster of $\Gamma 2^l \times \Gamma 2^l$ DEM pixels. The minimum number is $\Gamma \times \Gamma$. To integrate the two grids, step functions with a joint continuous domain are defined. The step functions are based on indicator functions, χ_P and χ_Ω, and P and Ω are sub-domains (Figures 1 and 2) defined as

$$P_{i,j} = [(i-1)\delta x,\ i\delta x] \times [(j-1)\delta x,\ j\delta x]$$

$$\Omega_{l,m,n} = [(m-1)\Delta x_l,\ m\Delta x_l] \times [(n-1)\Delta y_l,\ n\Delta y_l]$$

The definition of an indicator function for domain D is

$$\chi_D = \begin{cases} 1 \text{ if } (x,\ y) \in D \\ 0 \text{ if } (x,\ y) \notin D \end{cases}$$

This allows the following approximating functions with a continuous domain (Figure 3)

$$\tilde{e}(x,\ y) \approx e(x,\ y)$$

$$\tilde{e}(x,\ y) = \sum_{i=1}^{I} \sum_{j=1}^{J} e_{i,j} \chi_{P_{i,j}}(x,\ y)$$

$$\tilde{\zeta}(x,\ y,\ t) \approx \zeta(x,\ y,\ t)$$

$$\tilde{\zeta}(x,\ y,\ t) = \sum_{m=1}^{M} \sum_{n=1}^{N} \zeta_{l,m,n}(t) \chi_{\Omega_{l,m,n}}(x,\ y)$$

$$\tilde{h}(x,\ y,\ t) \approx h(x,\ y,\ t)$$

$$\tilde{h}(x,\ y,\ t) = \max\left[0,\ \tilde{\zeta}(x,\ y,\ t) - \tilde{e}(x,\ y)\right]$$

Here

$$\zeta_{l,m,n} \approx \zeta[(m-1/2)\Delta x_l,\ (n-1/2)\Delta y_l,\ t]$$

The quarter sub-domains are also defined by compass direction (Figure 4) as

$$\Omega^{\mathrm{SW}}_{l,m,n} = [(m-1)\Delta x_l,\ (m-1/2)\Delta x_l] \times [(n-1)\Delta y_l,\ (n-1/2)\Delta y_l]$$

$$\Omega^{\mathrm{NW}}_{l,m,n} = [(m-1)\Delta x_l,\ (m-1/2)\Delta x_l] \times [(n-1/2)\Delta y_l,\ n\Delta y_l]$$

$$\Omega^{\mathrm{NE}}_{l,m,n} = [(m-1/2)\Delta x_l,\ m\Delta x_l] \times [(n-1/2)\Delta y_l,\ n\Delta y_l]$$

$$\Omega^{\mathrm{SE}}_{l,m,n} = [(m-1/2)\Delta x_l,\ m\Delta x_l] \times [(n-1)\Delta y_l,\ (n-1/2)\Delta y_l]$$

A quadtree can be considered as a grid with a hierarchical ordering (Figure 5) with cells as leaves at different levels l in the hierarchy. For the domains of the computational cells at different leaf levels

$$\Omega_{l-1,2m-1,2n-1} = \Omega^{\mathrm{SW}}_{l,m,n},\ \Omega_{l-1,2m,2n-1} = \Omega^{\mathrm{SE}}_{l,m,n},$$
$$\Omega_{l-1,2m-1,2n} = \Omega^{\mathrm{NW}}_{l,m,n},\ \Omega_{l-1,2m,2n} = \Omega^{\mathrm{NE}}_{l,m,n}$$

To get a 'balanced quadtree', the maximum difference in leaf layer number between two adjacent cells is 1. Velocity domains in the staggered grid (Figures 6 and 7), denoted as $\Omega_{l,m+1/2,n}$ or $\Omega_{l,m,n+1/2}$, depend on the leaf layer difference between two adjacent volume cells. In general, we have

$$\Omega_{l,m+1/2,n} = \Omega^{\mathrm{E}} + \Omega^{\mathrm{W}} \quad \text{at } (l,\ m+1/2,\ n)$$

For $\Omega^{\mathrm{E,W}}_{l,m+1/2,n}$ the following options exist

$$\Omega^{\mathrm{E}} = \begin{cases} \Omega^{\mathrm{NW}}_{l+1,(m/2)+1,n/2)} & l^{\mathrm{E}} > l, \quad n = \text{even} \\ \Omega^{\mathrm{SW}}_{l+1,(m/2)+1,(n+1)/2} & l^{\mathrm{E}} > l, \quad n = \text{odd} \\ \Omega^{\mathrm{SW+NW}}_{l,m+1,n} & l^{\mathrm{E}} = l \end{cases}$$

$$\Omega^{\mathrm{W}} = \begin{cases} \Omega^{\mathrm{NE}}_{l+1,m/2,n/2} & l^{\mathrm{W}} > l, \quad n = \text{even} \\ \Omega^{\mathrm{SE}}_{l+1,m/2,(n+1)/2} & l^{\mathrm{W}} > l, \quad n = \text{odd} \\ \Omega^{\mathrm{SW+NW}}_{l,m,n} & l^{\mathrm{W}} = l \end{cases}$$

4.

(see also Figures 6 and 7). This implies that each domain of the momentum volumes can always be composed of quarter sub-domains. If there is no level difference between adjacent volumes, the number of quarter sub-domains is $2 + 2 = 4$, other-

wise it is $1 + 2 = 3$. Flooding and drying might change these numbers due to completely dry quarters.

The following discrete variables are then defined as follows.

Cross-section

$$A^x_{l,m+1/2,n}(t) = \int_{(n-1)\Delta y_l}^{n\Delta y_l} \tilde{h}(m\Delta x_l,\ y,\ t)\,\mathrm{d}y$$

Cross-section

$$A^y_{l,m,n+1/2}(t) = \int_{(m-1)\Delta x_l}^{m\Delta x_l} \tilde{h}(x,\ n\Delta y_l,\ t)\,\mathrm{d}x$$

'Water level volume'

$$V_{l,m,n}(t) = \iint_{\Omega_{l,m,n}} \tilde{h}(x,\ y,\ t)\,\mathrm{d}x\,\mathrm{d}y$$

(see Figure 3)

'Velocity volume'

$$V_{l,m+1/2,n}(t) = \iint_{\Omega_{l,m+1/2,n}} \tilde{h}(x,\ y,\ t)\,\mathrm{d}x\,\mathrm{d}y$$

Volume-averaged velocity

$$u_{l,m+1/2,n}(t) \approx \frac{\iint_{\Omega_{l,m+1/2,n}} u(x,\ y,\ t)\,h(x,\ y,\ t)\,\mathrm{d}x\,\mathrm{d}y}{\iint_{\Omega_{l,m+1/2,n}} h(x,\ y,\ t)\,\mathrm{d}x\,\mathrm{d}y}$$

Discharge in x-direction

$$Q^x_{l,m+1/2,n}(t) = A^x_{l,m+1/2,n}(t)\,u_{l,m+1/2,n}(t)$$

Due to the step functions, the integrals above are in fact only simple summations

$$V_{l,m,n}(t) = \iint_{\Omega_{l,m,n}} \tilde{h}(x,\ y,\ t)\,\mathrm{d}x\,\mathrm{d}y = \delta x^2 \sum_{i=i_0}^{i=i_1} \sum_{j=j_0}^{j=j_1} \max(0,\ \zeta_{l,m,n} - e_{i,j})$$

in which

$$i_0 = 2^l\Gamma(m-1) + 1$$

$$i_1 = 2^l\Gamma m$$

$$j_0 = 2^l\Gamma(n-1) + 1$$

$$j_1 = 2^l\Gamma n$$

Cross-sections at the interfaces of cells are slightly more complex and are given by

$$A^y_{l,m,n+1/2}(t) = \int_{(n-1)\Delta y_l}^{n\Delta y_l} \tilde{h}(m\Delta x_l,\ y,\ t)\,\mathrm{d}y = \delta x \sum_{j=j_0}^{j=j_1} \max(0,\ {}^*\zeta_{l,m+1/2,n} - e_{i+1/2,j})$$

where

$$i = 2^l\Gamma m$$

$$j_0 = 2^l\Gamma(n-1) + 1$$

$$j_1 = 2^l\Gamma n$$

Here we have

$$e_{i+1/2,j} = \max(e_{i,j},\ e_{i+1,j})$$

and, for ${}^*\zeta$, we apply first-order upwinding

$${}^*\zeta_{l,m+1/2,n} = \max\left(0,\ \frac{u_{l,m+1/2,n}}{|u_{l,m+1/2,n}|}\right)\zeta_{l,m,n} - \min\left(0,\ \frac{u_{l,m+1/2,n}}{|u_{l,m+1/2,n}|}\right)\zeta_{l,m+1,n}$$

2.2 The finite-volume equations

The equations are derived from the shallow water equations. The finite-volume formulation is as follows. The continuity equation is

$$V_t + \sum_{\partial\Omega} Q\boldsymbol{n}_f = 0 \quad \text{at } (l,\ m,\ n) \tag{5}$$

where V at $(l, m, n) = V_{l,m,n}$, $\sum_{\partial\Omega}$ denotes the summation of discharges over all the faces of $\Omega_{l,m,n}$ and $\boldsymbol{n}_f$ is the outward directed normal. The actual number of discharges depends on the local quadtree ordering.

The momentum equation is

$$(uV)_t + \sum_{\partial\Omega} {}^{*}u\bar{Q}\boldsymbol{n}_f + \iint_{\Omega} \tilde{h} g D_x\zeta + \iint_{\Omega} \tau_{\mathrm{b}}^{u}/\rho = 0 \quad \text{at } (l,\ m+1/2,\ n) \tag{6a}$$

in which ρ is density, τ_{b} is bottom friction and $D_x\zeta$ is the free surface gradient. ${}^{*}u$ is computed by upwinding and the discharge $\bar{Q}$ has to be estimated by an averaging procedure. (Since the momentum equation for v in the y-direction is exactly similar, we ignore that equation.) After application of $(uV)_t = u_t V + uV_t$, dividing by V and normalising the bottom friction as $\hat{\tau} = \tau/\rho$, Equation (6a) can be rewritten as

$$u_t + \frac{\overbrace{\sum_{\partial\Omega} {}^{*}u\bar{Q}\boldsymbol{n}_f + uV_t}^{\text{advection}}}{V} + \frac{\overbrace{\iint_{\Omega} \tilde{h} g D_x\zeta}^{\text{hydrostatic pressure}}}{V} + \frac{\overbrace{\iint_{\Omega} \hat{\tau}_{\mathrm{b}}^{u}}^{\text{bottom friction}}}{V} = 0 \quad \text{at } (l,\ m+1/2,\ n) \tag{6b}$$

The spatial discretisation for each component is now described.

2.2.1 Hydrostatic pressure

The normalised force due to hydrostatic pressure is given by

$$-\hat{F}^{x}_{\text{hydrostatic pressure}} = \iint_{\Omega} \tilde{h} g D_x\zeta$$

The hydrostatic pressure gradient, $D_x\zeta$, is assumed to be constant within $\Omega_{l,m+1/2,n}$. This implies

$$\iint_{\Omega} \tilde{h} g D_x\zeta = g D_x\zeta \iint_{\Omega} \tilde{h} = g D_x\zeta V$$

or

$$-\frac{\hat{F}^{x}_{\text{hydrostatic pressure}}}{V} = g D_x\zeta = \frac{\zeta^{\mathrm{E}} - \zeta^{\mathrm{W}}}{(\Delta x^{\mathrm{E}} + \Delta x^{\mathrm{W}})/2} \quad \text{at } (l,\ m+1/2,\ n) \tag{7}$$

where the values for $\zeta^{\mathrm{E,W}}$ at $(l, m+1/2, n)$ (see Figure 7) depend on the quadtree as follows.

$$\zeta^{\mathrm{E}} = \zeta_{l,m+1,n},\ \zeta^{\mathrm{W}} = \zeta_{l,m,n},\ l^{\mathrm{E}} = l^{\mathrm{W}}$$

$$\zeta^{\mathrm{E}} = \zeta_{l+1,(m/2)+1,n/2},\ \zeta^{\mathrm{W}} = \frac{\zeta_{l,m,n} + \zeta_{l,m,n-1}}{2}$$
$$n = \text{even and } l^{\mathrm{E}} > l^{\mathrm{W}}$$

$$\zeta^{\mathrm{E}} = \zeta_{l+1,(m/2)+1,(n+1)/2},\ \zeta^{\mathrm{W}} = \frac{\zeta_{l,m,n} + \zeta_{l,m,n+1}}{2}$$
$$n = \text{odd and } l^{\mathrm{E}} > l^{\mathrm{W}}$$

$$\zeta^{\mathrm{E}} = \frac{\zeta_{l,m+1,n} + \zeta_{l,m+1,n-1}}{2},\ \zeta^{\mathrm{W}} = \zeta_{l+1,m/2,n/2}$$
$$n = \text{even and } l^{\mathrm{E}} < l^{\mathrm{W}}$$

$$\zeta^{\mathrm{E}} = \frac{\zeta_{l,m+1,n} + \zeta_{l,m+1,n+1}}{2},\ \zeta^{\mathrm{W}} = \zeta_{l+1,m/2,(n+1)/2}$$
$$n = \text{odd and } l^{\mathrm{E}} < l^{\mathrm{W}}$$

2.2.2 Bottom friction

The bottom friction force follows from the surface integral of τ_{b}

$$-\hat{F}^{\mathrm{x}}_{\text{bottom friction}} = \iint_{\Omega} \hat{\tau}_{\mathrm{b}}^{u} = \iint_{\Omega} c^{\mathrm{f}} u \|u\|$$

where c^{f} is a dimensionless coefficient based on formulations such as Manning or Chezy (e.g. Yen, 2002). Within $\Omega_{l,m+1/2,n}$ we do not know u. One might assume a constant velocity $u_{l,m+1/2,n}$. However, for gravity-driven flow, in shallow areas with locally relative deep pixels, such as ditches (see Figure 8), this will

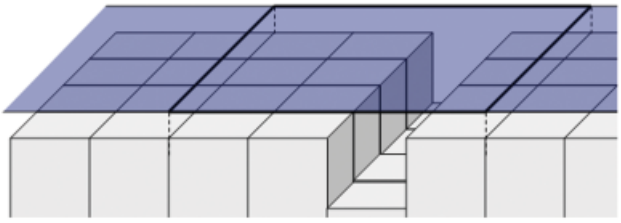

Figure 8. Sub-grid ditch

overestimate friction and underestimate conveyance. (For dominantly wind-driven flow the assumptions of this section are not valid, and constant velocity would be a better assumption.) Instead, we try to construct a function $\tilde{u}(x, y)$. This function is based on two assumptions valid within a quarter of a computational cell.

(*a*) The friction slope S^{f} is constant.
(*b*) The direction of the flow is constant.

For $\Omega = \Omega_{l,m,n}^{\mathrm{SW},\ldots,\mathrm{NE}}$, this gives the following expressions.

$$\left|S^{\mathrm{f}}\right| = \frac{\tilde{u}(x, y)^2 + \tilde{v}(x, y)^2}{g\tilde{h}/c^{\mathrm{f}}} = \frac{c^{\mathrm{f}}\|\tilde{u}\|^2}{g\tilde{h}}$$

$$= \text{constant if } (x, y) \in \Omega \tag{8}$$

$$\|\tilde{u}\| = \frac{\iint_{\Omega} \tilde{h}(\tilde{u}^2 + \tilde{v}^2)^{1/2}}{V} = \frac{\iint_{\Omega} \tilde{h}\|\tilde{u}\|}{V}$$

at SW, ..., NE of (l, m, n)

This implies

$$\|\tilde{u}(x, y)\| = \|\tilde{u}(x', y')\| \frac{(\tilde{h}/c^{\mathrm{f}})^{1/2}}{(\tilde{h}'/c^{\mathrm{f}'})^{1/2}}$$

$$\text{if } (x, y) \in \Omega \text{ and } (x', y') \in \Omega,\ \tilde{h}' = \tilde{h}(x', y') \tag{9}$$

We further assume

$$\|\tilde{u}(x', y')\| = \frac{\|u\|}{\alpha(x', y')}$$

where, for instance

$$u = u_{l,m,n}^{\mathrm{NE}} = \begin{cases} u_{l,m+1/2,n} \\ \text{or} \\ u_{l-1,2m+1/2,2n} \end{cases}$$

$$v = v_{l,m,n}^{\mathrm{NE}} = \begin{cases} v_{l,m,n+1/2} \\ \text{or} \\ v_{l-1,2m,2n+1/2} \end{cases}$$

It follows that

$$\alpha' = \frac{\|u\|}{\|\tilde{u}'\|} = \frac{\iint_{\Omega} \|\tilde{u}\|\tilde{h}}{\|\tilde{u}'\|V} = \frac{\|\tilde{u}'\|\iint_{\Omega} \tilde{h}(\tilde{h}/c^{\mathrm{f}})^{1/2}}{\|\tilde{u}'\|(\tilde{h}'/c^{\mathrm{f}'})^{1/2}V}$$

$$= \left(\frac{c^{\mathrm{f}'}}{\tilde{h}'}\right)^{1/2} \frac{\iint_{\Omega} \tilde{h}(\tilde{h}/c^{\mathrm{f}})^{1/2}}{V} \tag{10}$$

The x-component of the bottom friction in a cell quarter is now given by

$$-\hat{F}_{\mathrm{b}}^{x} = u\|u\| \iint_{\Omega} \frac{c^{\mathrm{f}}}{\alpha^2} = u\|u\| \frac{V^3}{\left[\iint_{\Omega} \tilde{h}(\tilde{h}/c^{\mathrm{f}})^{1/2}\right]^2}$$

at SW, ..., NE of (l, m, n) (11)

Equation 11 can be written as

$$-(\hat{F}_{\mathrm{b}}^{x}) = Vu\|u\|/h^{\mathrm{f}},\ h^{\mathrm{f}} = \left[\frac{\iint_{\Omega} \tilde{h}(\tilde{h}/c^{\mathrm{f}})^{1/2}}{V}\right]^2$$

at SW, ..., NE of (l, m, n) (12)

We define h^{f} as the roughness depth. This is similar to effective depth (Defina, 2000; Yu and Lane, 2006b), but in our definition the spatial variation of c^{f} is taken into account as well. In the limiting case of only one pixel in a coarse cell, $h^{\mathrm{f}} = h/c^{\mathrm{f}}$. The total friction force in the x-direction depends on the local quadtree. For the simple case that $l^{\mathrm{E}} = l^{\mathrm{W}}$ it is given by

$$-\left(\frac{\hat{F}_{\mathrm{b}}^{x}}{V}\right)_{l,m+(1/2),n} = \frac{(\hat{F}_{\mathrm{b}}^{x})_{l,m+(1/2),n}^{\mathrm{W+E}}}{-V_{l,m+(1/2),n}}$$

$$= \frac{(\hat{F}_{\mathrm{b}}^{x})_{l,m,n}^{\mathrm{NE+SE}} + (\hat{F}_{\mathrm{b}}^{x})_{l,m+1,n}^{\mathrm{NW+SW}}}{-V_{l,m+(1/2),n}}$$

$$= \frac{u_{l,m+(1/2),n}}{V_{l,m+(1/2),n}} \left(f_{l,m,n}^{\mathrm{NE+SE}} + f_{l,m+1,n}^{\mathrm{NW+SW}}\right) \tag{13}$$

where

$$f = V\frac{\|u\|}{h^{\mathrm{f}}}$$

We define f as a friction factor since $\hat{F}_{\mathrm{b}}^{x} = uf$ and $\hat{F}_{\mathrm{b}}^{y} = vf$. By computing this friction factor per quarter of a grid cell, one can

easily compose any bottom friction force according to the sub-domain division as given by Equation 4. For instance, under the assumption that $l^{\mathrm{N}} = l^{\mathrm{S}}$, we get

$$-\left(\frac{\hat{F}_{\mathrm{b}}^{y}}{V}\right)_{l,m,n+(1/2)} = \frac{(\hat{F}_{\mathrm{b}}^{x})_{l,m,n+(1/2)}^{\mathrm{S+N}}}{-V_{l,m,n+(1/2)}} = \frac{v_{l,m,n+(1/2)}}{V_{l,m,n+(1/2)}}\left(f_{l,m,n}^{\mathrm{NW+NE}} + f_{l,m,n+1}^{\mathrm{SW+SE}}\right)$$

For large DEMs with many pixels per grid cell, the evaluation of friction factors might be expensive in terms of processor and memory requirements. For efficient evaluation it is convenient to make use of tables combined with Taylor series (see the appendix).

2.2.3 Advection of momentum

$$-\hat{F}_{\mathrm{advection}}^{x} = \sum_{f} {}^{*}u\bar{Q}\boldsymbol{n}_f + uV_t$$

The values for ${}^{*}u$ are simply computed by upwinding. The remaining problem is the computation of the discharges $\bar{Q}$ at the faces of $\Omega_{l,m+1/2,n}$ (see Figure 9) such that

$$V_t + \sum_{f} \bar{Q}\boldsymbol{n}_f = 0$$

14. at $(l,\ m+1/2,\ n)$ or at $(l,\ m,\ n+1/2)$

First we compute the discharges at the faces of each sub-volume with the domains $\Omega_{m,n}^{\mathrm{SW,\ldots,NE}}$. By constructing a velocity volume as the summation of adjacent sub-volumes, according to Equation 4, we will get the discharges at the faces of $V_{l,m+1/2,n}$ automatically. The sub-grid discharges are computed by the assumption

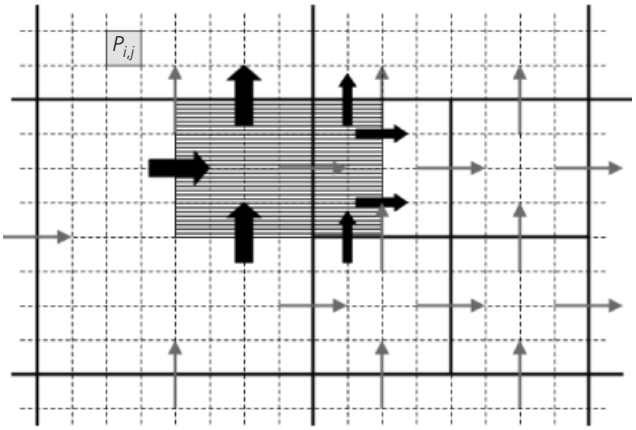

Figure 9. Discharges for momentum transport

15. $$(V_{l,m,n}^{\mathrm{SW}})_t = \bar{Q}_{l,m-1/2,n}^{x,0} - \bar{Q}_{l,m,n}^{x,0} + \bar{Q}_{l,m,n-1/2}^{y,0} - \bar{Q}_{l,m,n}^{y,0}$$

In this equation there are two external discharges at the external face of $V_{l,m,n}$, $\bar{Q}_{m-1/2,n}^{x,0}$ and $\bar{Q}_{m,n-1/2}^{y,0}$ (Figure 5), and two internal discharges, $\bar{Q}_{m,n}^{x\,\mathrm{or}\,y,0}$. Assuming

$$\bar{\boldsymbol{u}}_{m-1/2,n}^{0} = \bar{\boldsymbol{u}}_{m-1/2,n}^{1} = u_{m-1/2,n}$$

yields

16. $$\bar{Q}_{l,m-1/2,n}^{x,0} = u_{l,m-1/2,n}\int_{(n-1)\Delta y_l}^{(n-1/2)\Delta y_l} \tilde{h}[(m-1)\Delta x_l,\ y]\,\mathrm{d}y$$

where we integrate over a sub-face. Likewise, $\bar{Q}_{l,m,n-1/2}^{y,0}$ can be computed. For the internal discharges, $\bar{Q}_{m,n}^{u,0}$ and $\bar{Q}_{m,n}^{v,0}$, we need four equations for $(V_{m,n}^{\mathrm{SW,\ldots,NE}})_t$ with the four unknowns $\bar{Q}_{l,m,n}^{x,0}$, $\bar{Q}_{l,m,n}^{x,1}$, $\bar{Q}_{l,m,n}^{y,0}$ and $\bar{Q}_{l,m,n}^{y,1}$. However, Equation 15 applied for SW, …, NE is an identical system with no unique solution. To solve this, we replace one equation by the requirement that the expression

$$E_Q = (\bar{Q}^{x,0}/A^{x,0})^2 + (\bar{Q}^{x,1}/A^{x,1})^2 + (\bar{Q}^{y,0}/A^{y,0})^2 + (\bar{Q}^{y,1}/A^{y,1})^2 \quad \text{at } (l,\ m,\ n)$$

should be minimal. The fourth equation can now be found by a linear least-squares procedure. After this we can write

$$-\hat{F}_{\mathrm{advection}}^{x} = \sum_{f} {}^{*}u\bar{Q}\boldsymbol{n}_f + uV_t = \sum_{f} {}^{*}u\bar{Q}\boldsymbol{n}_f - u\sum_{f}\bar{Q}\boldsymbol{n}_f = \sum_{f}({}^{*}u - u)\bar{Q}\boldsymbol{n}_f$$

First-order upwinding at outflow locations yields ${}^{*}u = u$. So this expression implies the summation of inflowing momentum discharges only. We now define

17. $$\mathrm{adv}(u) = \frac{1}{V}\sum_{f}({}^{*}u - u)\bar{Q}\boldsymbol{n}_f$$

At strong flow contractions, a correction (Stelling and Duinmeijer, 2003) has to be applied to correct for head gain due to shortcomings locally of the hydrostatic assumption.

In summary, we get the following spatial discretisation of the momentum equations

$$u_t + \mathrm{adv}(u) + gD_x\zeta + \frac{u}{V} f^{\mathrm{W+E}} = 0$$

6c. at $(l,\ m + 1/2,\ n)$

2.3 Semi-implicit time integration

Time integration is based on the θ method in combination with a predictor–corrector approach for the bottom friction. This is required in the case of large-area flooding problems. The time integration is given by

$$\frac{V(\zeta^{k+1}) - V(\zeta^k)}{\Delta t} + \sum_f A^k u^{k+\theta} \boldsymbol{n}_f = 0$$

at $(l,\ m,\ n)$

18. $u^{k+\theta} = (1-\theta)u^k + \theta u^{k+1}$

$$\frac{u^{k+1} - u^k}{\Delta t} + \mathrm{adv}(u^k) + gD_x\zeta^{k+\theta} + \frac{u^{k+1}}{V^k}(f^k)^{\mathrm{E+W}} = 0$$

19. at $(l,\ m+1/2,\ n)$ $(l^{\mathrm{E}} = l^{\mathrm{W}})$

Due to the sub-grid approach, the strict mass-conserving continuity equation is non-linear. After elimination of u^{k+1} from Equation 18 by substitution of Equation 19, we follow an iterative approach (Casulli, 2009) based on Newton iteration, which includes flooding and drying. The method is based on V as a non-linear function that is strictly positive. Now the implicit time integration adjusts the water levels to the positivity of V. Implicit time integration is imperative for this procedure.

If $l^{\mathrm{E}} \neq l^{\mathrm{W}}$, the pressure gradient is different from Equation 19. According to Equation 4, we have four options in this case; just one example is given here

$$D_x\zeta = \frac{\zeta_{l+1,m/2+1,n/2} - (\zeta_{l,m,n} + \zeta_{l,m,n-1})/2}{(\Delta x_{l+1} + \Delta x_l)/2}$$

$$n = \text{even and } l^{\mathrm{E}} > l^{\mathrm{W}}$$

This expression is rewritten as

$$D_x\zeta = \frac{\zeta_{l+1,m/2+1,n/2} - \zeta_{l,m,n}}{(\Delta x_{l+1} + \Delta x_l)/2} + \frac{\zeta_{l,m,n} - \zeta_{l,m,n-1}}{\Delta x_{l+1} + \Delta x_l}$$
$$= D_x\zeta - d_y\zeta + d_y\zeta$$

The time integration is given by

$$\frac{u^{k+1} - u^k}{\Delta t} + \mathrm{adv}(u^k) + g(D_x - d_y)\zeta^{k+\theta} + d_y\zeta^k + \frac{u^{k+1}}{V^k}(f^k)^{\mathrm{W+E}} = 0$$

20a. at $(l,\ m+1/2,\ n,\ n = \text{even})$

$$\frac{u^{k+1} - u^k}{\Delta t} + \mathrm{adv}(u^k) + g(D_x + d_y)\zeta^{k+\theta} - d_y\zeta^k + \frac{u^{k+1}}{V^k}(f^k)^{\mathrm{W+E}} = 0$$

20b. at $(l,\ m+1/2,\ n,\ n = \text{odd})$

In this way, the requirements of a positive definite and symmetric system of equations to apply the conjugate gradient method for the linear equations are fulfilled (Casulli and Walters, 2000). In fact, the method that we use is a combination of Gaussian elimination and the Conjugate Gradient method; see Kernkamp *et al.* (2011). The anti-symmetry of the system between odd numbered and even numbered momentum equations avoids stability problems due to the explicit $d_y\zeta^k$ term. The advection approximation imposes the velocity Courant-Friedrichs-Lewy condition. This can be bypassed by a locally implicit method (Kramer and Stelling, 2008). Neglecting advection as well as inertia yields the diffusive wave approximation (e.g. Bates and De Roo, 2000; Yu and Lane, 2011), which is unconditionally stable for this time integration.

3. Examples

The method described here is based on developments over many years. Without sub-grids or quadtrees, it has been intensively tested and applied, with structured and unstructured grids, both for theoretical test cases and practical applications. Theoretical test cases such as classical dam breaks and hydraulic jumps can be found in works by Stelling and Duinmeijer (2003), Kramer and Stelling (2008), Zijlema and Stelling (2008) and Kernkamp *et al.* (2011). For flat bottoms without quadtrees, the method described here is exactly the same. A theoretical test case for flooding and drying with the sub-grid method is given by Casulli (2009). A comparison with real floods, based on historic flood events, is described by Hesselink *et al.* (2003). Practical applica-

tions, without sub-grids and quadtrees, are given by Alkema and Middelkoop (2005), Carrivick (2006), Tarekegn *et al.* (2010), Kernkamp *et al.* (2011) and Poretti and De Amicis (2011), among others. Flooding test cases with the combination of 1D channels embedded in 2D terrains, both based on Stelling and Duinmeijer (2003), can be found in the work of Stelling and Verwey (2005). Two test examples that highlight the sub-grid, the bottom friction and the quadtree are described here. The first example shows the efficiency of the sub-grid for accuracy in bathymetry combined with friction. The second shows the efficiency of quadtrees for the representation of dykes that might break or overflow.

3.1 U-bend

The first example considers a U-bend (Figure 10); this river section has a deep outer bend, a shallow inner bend and a bed slope of $2{\cdot}0 \times 10^{-4}$. The bottom cross-section is a quarter period of a sinusoidal function with an amplitude of 4 m (Figure 10). The minimum inner radius of the bend, for the highest water levels is 107 m. The outer radius is 320 m. The maximum width is 213 m. This varies with water level. We assume a uniform Manning coefficient of 0·026. The sub-grid is very detailed with a pixel size of 1×1 m and a total number of 960×640 pixels. The outer bend position is fixed, but the inner bend position depends on the water level. At both inflow and outflow, water levels are imposed as boundary conditions. The maximum water depth is kept the same at both inflow and outflow. The resulting river discharge can be considered as the equilibrium discharge for the given water depth. We consider combinations of different coarse grid sizes and different prescribed water depths. The coarsest and finest grids are shown in Figure 11. The results of the combinations are summarised in Table 1.

In particular, the grid $dx_0 = 80$ m is very coarse. Nonetheless, the equilibrium discharges for all three cases are very close to each other, as Table 1 shows. The sub-grid gives a similar accuracy as cut cells (Rosatti *et al.*, 2005). The combination with the friction approach based on roughness depth yields a very accurate result given the relative very coarse grid. Figure 12 shows the wet bed for the highest water level and a number of streamlines. Figure 13 plots the interpolated water levels along the streamlines in the inner and outer bend. For the straight sections, the horizontal scale is based on a dimensionless distance along the streamline, scaled from 0 to 1 and from 2 to 3. The bend in the middle section is plotted based on the angle of polar coordinates in the bend, ranging from 0 to π and scaled from 1 to 2. This allows plotting of the water levels along the streamlines, which are

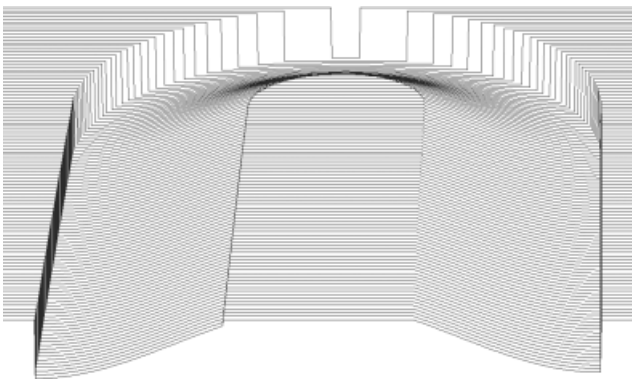

Figure 10. River bend bottom

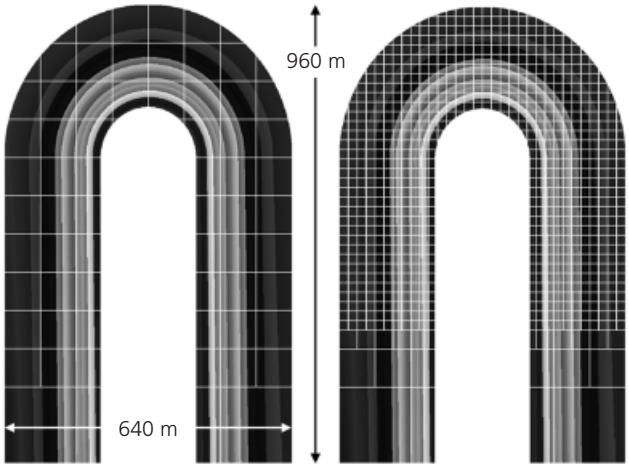

Figure 11. Coarsest and finest grids for river bend

dx_0: m	$Q_{equilibrium}$: m^3/s		
	E1 $h_{max} = 3{\cdot}9$ m	E2 $h_{max} = 1{\cdot}9$	E3 $h_{max} = 0{\cdot}9$
80	539·0	106·1	20·2
40	546·1	106·9	20·2
20	550·0	107·4	20·2

Table 1. Comparison of discharges

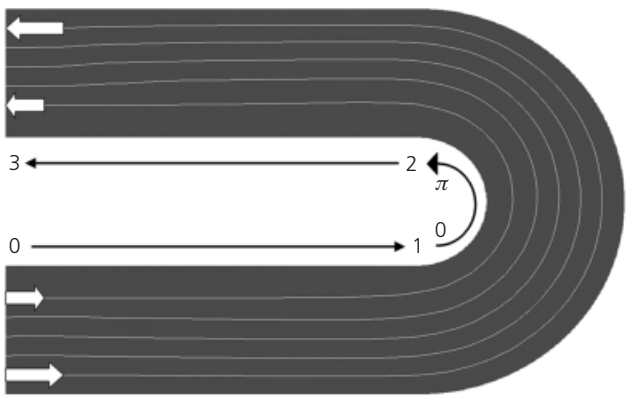

Figure 12. River bend flow, $h_{max} = 4$ m

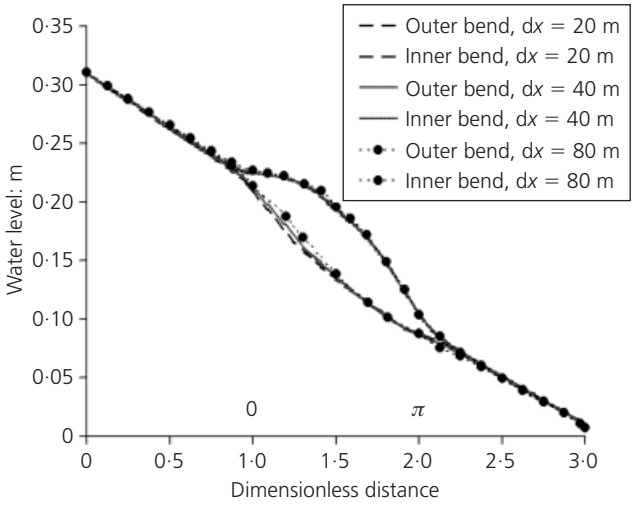

Figure 13. Comparison of water levels

different in length, on the same horizontal scale. The effect of momentum advection in the river bend is only significant for case E1. The results for the three different grids are still quite similar and show the remarkable accuracy of this approach.

Figure 14 shows the wet bed for the coarse grid and the lowest water level. For all cases, the wet beds are all the same, regardless of grid size.

3.2 Flooding case

A practical example shows the efficiency of this method due to the quadtree with sub-grid extension. This example concerns a polder area in the north of the Netherlands, near the village of Petten, where there is no protection by dunes, only a dyke against storm surges at sea. Consider a dyke failure with a breach of 160 m width. A DEM is used with pixels of 5×5 m. In the case of polder flooding, it is important to represent accurately obstacles that might block the flow, such as dykes and roads. With a minimum coarse grid size of four pixels, obstacles cannot be missed. Figure 15 shows the grid and Figure 16 shows a

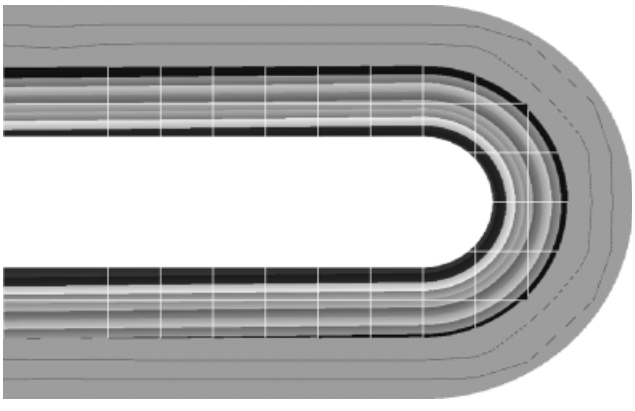

Figure 14. Wet bed low water level, d$x = 80$

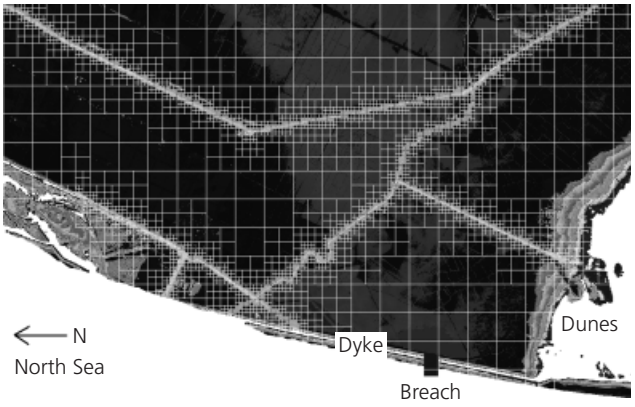

Figure 15. Quadtree grid with sub-grid

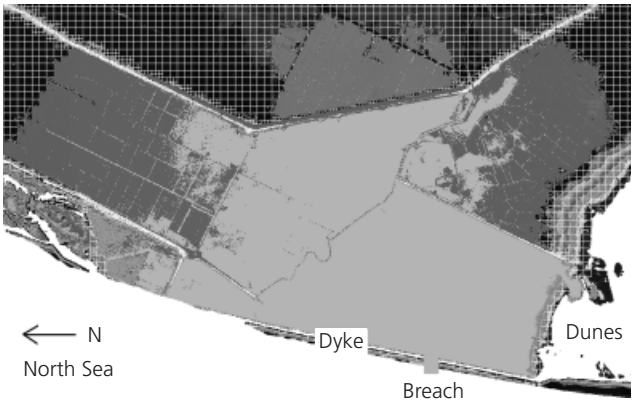

Figure 16. Snapshot of flooding event

snapshot after 5 h of flooding. The fine sub-grid contains $1386 \times 886 = 1\,227\,996$ pixels. Three coarse grids are considered: grid 1, $\Gamma = 4$, $l_{\max} = 4$; grid 2, $\Gamma = 2$, $l_{\max} = 5$; grid 3, $\Gamma = 2$, $l_{\max} = 3$. Grids 1–3 have 4880, 10 736 and 13 014 cells respectively – a factor 100 to 250 less than the number of pixels. Nevertheless, the sub-grid approach yields a detailed view (see Figure 16), while the grid is relatively coarse. The computational time on a simple laptop, for a simulation of 3 days, is less than 5 min. Without the sub-grid, an equally accurate simulation is often more than a 100 times slower.

The quadtree is not (yet) applied dynamically here. It is adapted to the location of dams and roads that might block the flow temporarily before they overflow. In that case, there is rapidly varying flow near the dams possibly with hydraulic jumps. Detailed grids are needed here to capture this automatically and accurately. The flow is directed normal to the crests. Some applications (Wang *et al.*, 2004) apply quadtrees for accurate representation of closed boundaries, where the flow is aligned with the boundary. In the current case, this is taken care of by the 'cut cell effect' of the sub-grid. Overland flows in low-land polders are not likely to propagate with significant bores, but the

case of hydro dam breaks is different. For those applications, quadtrees could be applied dynamically to refine near the bore front (Liang *et al.*, 2004).

Figure 17 shows inundated hectares as a function of hours for three different grids. Here, the sea level boundary condition was chosen at 3·5 m above normal level. Grids 2 and 3 give equal results, so the coarser grid at the relative flat polder area does not influence the results. Within 8 h, a large area is almost completely inundated. Grid 1 inundates a little bit slower. This is with local adaptation of the DEM such that the polder dams are recognised within the 4×4 pixel coarse grid size. Without this adjustment, the inundation proceeds too quickly, as shown in Figure 17. In other words, it is imperative to have an accurate representation of the dams.

More practical applications of the method can be viewed at www.3di.nu.

4. Concluding remarks

This paper has presented a novel approach based on a detailed DEM without the need for an evenly fine grid for flow quantities. The method has a number of advantages.

(*a*) It is efficient, producing accurate volumes and cross-sections regardless of the resolution of the coarse grid.
(*b*) The 2D extension of the 1D divided channel approach allows accurate representation of local roughness variation not only due to the bathymetry but also due to local variation of surface type (pavement versus vegetation for example).
(*c*) The method yields simple and efficient grid generation for quadtree coarse grids, connected to a high-resolution DEM, without the need for interpolation of depth values.
(*d*) Different grids of different resolution are all based on the same DEM; this allows very rapid assessment combined with detailed simulations.
(*e*) To reduce memory – and computational requirements – pre-computed tables might be used. This allows the analysis of DEMs with tens of millions of pixels on relatively simple computers.

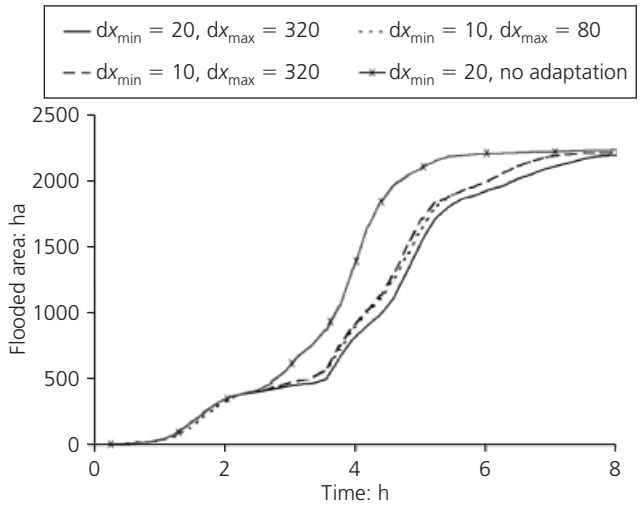

Figure 17. Time history of flooded hectares

Appendix. Tables for the evaluation of volumes and roughness depths

To reduce computational and memory requirements, tables can be used for the evaluation of volumes and bottom friction factors. Let us start with volumes.

$$V = \iint_{\Omega} \tilde{h} = \sum_{\Omega} \delta x^2 h_{i,j}$$

Consider two cases – case 1 ($\zeta \geqslant e^{\max}$) and case 2 ($e^{\min} < \zeta < e^{\max}$) where $e^{\max}$ is the maximum bottom elevation within a computational cell. For case 1, the number of wet pixels is fixed.

$$V = \sum_{\Omega} \delta x^2 h_{i,j} = \delta x^2 \sum_{\Omega} \zeta - \delta x^2 \sum_{\Omega} e_{i,j}$$
$$= \Delta x^2 \zeta - \delta x^2 \sum_{\Omega} e_{i,j} = \Delta x^2 \zeta - E$$

So, in this case, it is a simple formula where the number $E = \delta x^2 \sum \Omega e_{i,j}$ has to be computed only once at the start of the time integration. For case 2, the volume is a non-linear function since the number of wet pixels varies with depth. In this case, the volumes for various water levels are tabulated with a fixed increment of, for instance, 10 cm.

Bottom friction is less trivial. As an example, consider the Manning formula, given by

$$c^{\mathrm{f}} = \frac{g\mathbf{n}^2}{h^{1/3}}$$

where $\mathbf{n}$ denotes Manning's coefficient. According to Equation 13, friction factors are given by $f = V\|u\|/h^{\mathrm{f}}$ and these values have to be computed for every quarter of a grid cell. The volume is already dealt with, $\|u\|$ is trivial, so the computation of h^{f} is left. Substituting $c^{\mathrm{f}} = g\mathbf{n}^2/h^{1/3}$ into Equation 12 yields, with some rearrangement

$$(gh^f)^{1/2} = \frac{1}{V} \iint_{\Omega} \frac{\tilde{h}^{5/3}}{\mathbf{n}}$$

The volume V is known, so we look at $\iint_\Omega \tilde{h}^{5/3}/\mathbf{n}$. For case 1, $\zeta \geqslant e^{\max}$, we use a Taylor series as follows.

$$\iint_\Omega \frac{\tilde{h}^{5/3}}{\mathbf{n}} = \delta x^2 \sum_\Omega \frac{h_{i,j}^{5/3}}{\mathbf{n}_{i,j}}$$
$$= \delta x^2 \sum_\Omega \frac{1}{\mathbf{n}_{i,j}} \left(\overline{h}^{5/3} + \frac{5}{3}\Delta h_{i,j} \overline{h}^{2/3} + \frac{5}{9}\Delta h_{i,j}^2 \overline{h}^{-1/3} + \cdots \right)$$
$$\approx \delta x^2 \sum_\Omega \frac{\overline{h}^{-1/3}}{\mathbf{n}_{i,j}} \left(\overline{h}^2 + \frac{5}{3}\Delta h_{i,j} \overline{h} + \frac{5}{9}\Delta h_{i,j}^2 \right)$$

$\overline{h}$ and $\Delta h_{i,j}$ are defined as

$$\overline{h} = \zeta - \frac{\sum_\Omega e_{i,j}/\mathbf{n}_{i,j}}{\sum_\Omega 1/\mathbf{n}_{i,j}} = \zeta - \overline{e}$$

$$\Delta h_{i,j} = h_{i,j} - \overline{h} = \overline{e} - e_{i,j} = -\Delta e_{i,j}$$

Due to this definition of $\overline{h}$, as an average weighted with inverse Manning coefficients, we get

$$\sum_\Omega \Delta h_{i,j}/\mathbf{n}_{i,j} = 0$$

or

$$\iint_\Omega \frac{\tilde{h}^{5/3}}{\mathbf{n}} \approx \delta x^2 \sum_\Omega \frac{\overline{h}^{-1/3}}{\mathbf{n}_{i,j}} \left(\overline{h}^2 + \frac{5}{9}\Delta e_{i,j}^2 \right)$$
$$= \delta x^2 \overline{h}^{-1/3} \left(\overline{h}^2 \sum_\Omega \frac{1}{\mathbf{n}_{i,j}} + \frac{5}{9} \sum_\Omega \frac{\Delta e_{i,j}^2}{\mathbf{n}_{i,j}} \right)$$

All the summations in this expression can be part of the pre-processing before the actual flooding simulation. For case 2, $e^{\min} < \zeta < e^{\max}$, we simply set up a pre-computed table for the values of $\delta x^2 \sum \Omega h_{i,j}^{5/3}/\mathbf{n}_{i,j}$. In particular, if cells are relatively flat, as one often encounters in typical Dutch polder areas, the tables are rather small and a lot of memory space and computational effort is saved.

REFERENCES

Aftosmis MJ, Berger MJ and Melton JE (1998) Robust and efficient Cartesian mesh generation for component-based geometry. *AIAA Journal* **36(6)**: 952–960.

Alkema D and Middelkoop H (2005) The influence of floodplain compartmentalization on flood risk within the Rhine–Meuse Delta. *Natural Hazards* **36(1–2)**: 125–145.

Bates PD (2000) Development and testing of a sub-grid-scale model for moving boundary hydrodynamic problems in shallow water. *Hydrological Processes* **14(11–12)**: 2073–2088.

Bates PD and De Roo APJ (2000) A simple raster-based model for flood inundation simulation. *Journal of Hydrology* **236(1–2)**: 54–77.

Begnudelli L, Sanders BF and Bradford SF (2008) Adaptive Godunov-based model for flood simulation. *Journal of Hydraulic Engineering* **134(6)**: 714–725.

Brugnano L and Casulli V (2009) Iterative solutions of piecewise linear systems with applications to flows in porous media. *SIAM Journal on Scientific Computing* **31(3)**: 1858–1873.

Carrivick L (2006) Application of 2D hydrodynamic modelling to high-magnitude outburst floods: an example from Kverkfjoll, Iceland. *Journal of Hydrology* **321(1–4)**: 187–199.

Casulli V (2009) A high-resolution wetting and drying algorithm for free-surface hydrodynamics. *International Journal for Numerical Methods in Fluids* **60(4)**: 391–408.

Casulli V and Stelling GS (2011) Semi-implicit sub-grid modelling of three-dimensional free-surface flows. *International Journal for Numerical Methods in Fluids* **67(4)**: 441–449.

Casulli V and Walters RA (2000) An unstructured grid, three-dimensional model based on the shallow water equations. *International Journal for Numerical Methods in Fluids* **32(3)**: 331–348.

Causon DM and Ingram M (2001) A Cartesian cut cell method for shallow water flows with moving boundaries. *Advances in Water Resources* **24(8)**: 899–911.

Cea L and Vazquez-Cendon ME (2010) Unstructured finite volume discretization of two-dimensional depth-averaged shallow water equations with porosity. *International Journal for Numerical Methods in Fluids* **63(8)**: 903–930.

Defina A (2000) Two dimensional shallow flow equations for partially dry areas. *Water Resources Research* **36(11)**: 3251–3263.

Hesselink DM, Stelling GS, Kwadijk JCJ and Middelkoop H (2003) Inundation of a Dutch river polder, sensitivity analysis of a physically based model with historic data. *Water Resources* **39(9)**: article no. 1234.

Horritt DM and Bates PD (2001) Effects of spatial resolution on raster based models of flood flow. *Journal of Hydrology* **253(1–4)**: 239–249.

Kernkamp HWJ, van Dam A, Stelling GS and de Goede ED (2011) Efficient scheme for the shallow water equations on unstructured grids with application to the Continental Shelf. *Ocean Dynamics* **61(8)**: 1175–1188.

Kramer SC and Stelling GS (2008) A conservative unstructured scheme for rapidly varied flows. *International Journal for Numerical Methods in Fluids* **58(2)**: 183–212.

Liang Q, Borthwick AGL and Stelling GS (2004) Simulation of dam- and dyke-break hydrodynamics on dynamically

adaptive quadtree grids. *International Journal for Numerical Methods in Fluids* **46(2)**: 127–162.

Marks K and Bates P (2000) Integration of high-resolution topographic data with floodplain flow models. *Hydrological Processes* **14(11–12)**: 2109–2122.

Mittal R and Iaccarino G (2005) Immersed boundary methods. *Annual Review of Fluid Mechanics* **37**: 239–261.

Poretti I and De Amicis M (2011) An approach for flood hazard modelling and mapping in the medium Valtellina. *Natural Hazards and Earth System Sciences* **11(4)**: 1141–1151.

Rosatti G, Cesari D and Bonaventura L (2005) Semi-implicit, semi-Lagrangian modelling for environmental problems on staggered Cartesian grids with cut cells. *Journal of Computational Physics* **204(1)**: 353–377.

Sanders BF, Schubert JE and Gallegos HA (2008) Integral formulation of shallow-water equations with anisotropic porosity for urban flood modelling. *Journal of Hydrology* **362(1–2)**: 19–38.

Stelling GS and Duinmeijer SPA (2003) A staggered conservative scheme for every Froude number in rapidly varied shallow water flows. *International Journal for Numerical Methods in Fluids* **43(12)**: 1329–1354.

Stelling GS and Verwey A (2005) Numerical flood simulation. In *Encyclopedia of Hydrological Sciences* Vol. I, **doi**: 10.1002/0470848944.hsa025a.

Tarekegn TH, Haile AT, Rientjes T, Reggiani P and Alkema D (2010) Assessment of an ASTER-generated DEM for 2D hydrodynamic flood modelling. *International Journal of Applied Earth Observation and Geoinformation* **12(6)**: 457–465.

Wang JP, Borthwick AGL and Eatock Taylor R (2004) Finite-volume type VOF method on dynamically adaptive quadtree grids. *International Journal for Numerical Methods in Fluids* **45(5)**: 1–22.

Yen BC (2002) Open channel flow resistance. *Journal of Hydraulic Engineering* **128(1)**: 20–39.

Yu D and Lane SN (2006a) Urban fluvial flood modelling using a two-dimensional diffusion-wave treatment, part 1: mesh resolution effects. *Hydrological Processes* **20(7)**: 1541–1565.

Yu D and Lane SN (2006b) Urban fluvial flood modelling using a two-dimensional diffusion-wave treatment, part 2: development of a sub-grid-scale treatment. *Hydrological Processes* **20(7)**: 1567–1583.

Yu D and Lane SN (2011) Interactions between sub-grid-scale resolution, feature representation and grid-scale resolution in flood inundation modelling. *Hydrological Processes* **25(1)**: 36–53.

Zijlema M and Stelling GS (2008) Efficient computation of surf zone waves using the nonlinear shallow water equations with non-hydrostatic pressure. *Coastal Engineering* **55(10)**: 780–790.

WHAT DO YOU THINK?

To discuss this paper, please email up to 500 words to the editor at journals@ice.org.uk. Your contribution will be forwarded to the author(s) for a reply and, if considered appropriate by the editorial panel, will be published as a discussion in a future issue of the journal.

Proceedings journals rely entirely on contributions sent in by civil engineering professionals, academics and students. Papers should be 2000–5000 words long (briefing papers should be 1000–2000 words long), with adequate illustrations and references. You can submit your paper online via www.icevirtuallibrary.com/content/journals, where you will also find detailed author guidelines.